

Jimu LIU, Yuan TIAN, Feng GAO

A novel six-legged walking machine tool for *in-situ* operations

© The Author(s) 2020. This article is published with open access at link.springer.com and journal.hep.com.cn

Abstract The manufacture and maintenance of large parts in ships, trains, aircrafts, and so on create an increasing demand for mobile machine tools to perform *in-situ* operations. However, few mobile robots can accommodate the complex environment of industrial plants while performing machining tasks. This study proposes a novel six-legged walking machine tool consisting of a legged mobile robot and a portable parallel kinematic machine tool. The kinematic model of the entire system is presented, and the workspace of different components, including a leg, the body, and the head, is analyzed. A hierarchical motion planning scheme is proposed to take advantage of the large workspace of the legged mobile platform and the high precision of the parallel machine tool. The repeatability of the head motion, body motion, and walking distance is evaluated through experiments, which is 0.11, 1.0, and 3.4 mm, respectively. Finally, an application scenario is shown in which the walking machine tool steps successfully over a 250 mm-high obstacle and drills a hole in an aluminum plate. The experiments prove the rationality of the hierarchical motion planning scheme and demonstrate the extensive potential of the walking machine tool for *in-situ* operations on large parts.

Keywords legged robot, parallel mechanism, mobile machine tool, *in-situ* machining

1 Introduction

An increasing demand for manufacturing and maintaining large parts in several industrial fields, such as aeronautics, railroad, shipping, offshore platforms, and power plants, has emerged. Traditionally, large parts are generally

machined by large workspace machines [1]. In terms of maintenance and repair, a conventional approach involves disassembling the damaged parts of a system and shipping them to specialized workshops for processing, which is costly, complex, and time consuming. Furthermore, certain situations involve damaged parts that are impossible to disassemble; thus, maintenance relies on human workforce. Therefore, portable or mobile machine tools for performing *in-situ* post-production tasks for large parts are in demand.

Mobile manipulators have been studied for decades. The mobility of a manipulator can be provided by linear guide ways, wheeled or tracked vehicles, or legged robots. One of the most common mobile manipulators is a classical serial robot arm mounted on a wheeled mobile base [2]. MADAR is a dual-arm mobile manipulator with two commercial UR5 arms mounted on an omnidirectional platform. The mobile platform is driven by three specially designed omni-wheels that differ from commonly used Mecanum wheels [3]. KUKA AG demonstrated the polishing application of the mobile KMR QUANTEC robot in the aerospace industry. Apart from wheeled mobile platforms, parallel kinematic machine (PKM) tools are often mounted on gantry or crane support machines to perform material removal tasks, thereby combining the advantages of large travel ranges and high stiffness [4,5]. A track-based serial kinematic robot named SCOMPI was designed to perform *in-situ* processes, such as gouging, welding, grinding, hammer peening, and post-weld heat treating, for hydroelectric turbine maintenance. The track could be straight, circular, or a piece-wise sequence of circular track sections [6,7]. Moreover, a few mobile machines use a large-scale workpiece as a supporting structure. Several crawling portable robots have been designed to attach to fuselage or wing sections [8,9]. The Intersector Welding Robot was developed to conduct welding and machining processes while moving along rails mounted on the inner surface of the International Thermo-nuclear Experimental Reactor vacuum vessel sector [10].

Legged mobile robots are superior to wheeled and tracked robots in terms of terrain adaptability, as they can deal with isolated footholds and discontinuous terrains,

Received January 8, 2020; accepted April 23, 2020

Jimu LIU, Yuan TIAN, Feng GAO (✉)

State Key Laboratory of Mechanical System and Vibration, School of Mechanical Engineering, Shanghai Jiao Tong University, Shanghai 200240, China

E-mail: gaofengsjtu@gmail.com

such as stairs. A hydraulically driven six-legged robot named COMET-IV was developed to detect landmines and perform rescues in disaster areas [11]. Similarly, a motor-driven six-legged robot named SILO6 was designed to detect and remove antipersonnel landmines in infested fields [12]. CENTAURO is a wheeled-legged mobile manipulation platform capable of executing demanding manipulation tasks in disaster-response scenarios [13]. However, owing to the complexity of their mechanism and control as well as low stiffness, legged robots are rarely used in the industrial field. Only a limited number of legged robots have been developed for machining applications. Yang et al. [14] proposed an industry-oriented tripod robot that combines the mobility of legged robots and the advantages of parallel mechanisms. With lockers on certain passive joints and clamping devices at the end of limbs, the robot used only six actuators to perform locomotion tasks and manipulation tasks. REMORA is a reconfigurable quadruped robot with the same design philosophy [15]. Unlike the two aforementioned robots, which remain in the conceptual design stage, a robotic walking machine tool prototype named WalkingHex has been developed, and a set of experiments have shown its ability to perform *in-situ* machining operations [16,17]. The robot is a Stewart–Gough platform without a base platform that can perform machining tasks with all six feet attached to the floor. The top spherical joints of the robot can be actuated for the walking phase. However, the three-wire actuated spherical joint lacks an automated zeroing method and high motion accuracy. Hence, a calibration process, which takes approximately 10 min, is necessary when transitioning from the walking phase to the machining phase.

In terms of the kinematic design of manipulators, articulated arms are widely used. However, the low stiffness and precision of serial robot arms limit their application in light processing, such as welding, painting, and inspections. Therefore, PKMs for mobile machining have garnered increasing attention. Similar to the well-known Sprint Z3 head, a 3-degree of freedom (3-DOF) PKM module called the A3 head has been designed for large structural component machining [18]. Moreover, the dynamics and positional capability of the Fanuc F200iB hexapod robot have been investigated for mobile machining [19,20]. Another portable large-volume machine tool solution is the hybrid serial-parallel mechanism. A typical example is the Tricept machine, which has been successfully utilized in the aerospace industry [4]. Inspired by the Tricept, Huang et al. [21] designed a 4-DOF hybrid kinematic machine named Bicept comprising a 2-DOF parallel mechanism and a 2-DOF rotating head. Bicept was designed as a machine module moving along a long track for drilling and riveting in the assembly process of aircraft structural components. The high stiffness and precision advantages of parallel or hybrid-parallel kinematic

machine tools make them promising solutions for *in-situ* machining.

In this study, we introduce a novel six-legged walking machine tool developed to perform *in-situ* maintenance for large parts, such as trains, ships, and airplanes. Working environments may include certain obstacles or uneven terrain. Therefore, the walking machine tool is expected to demonstrate the following abilities: Can walk autonomously to a working area; can adapt to different types of terrain, including flats, slopes, and steps; and can perform machining operations on large parts. Its overall layout is similar to that of a classic mobile manipulator, that is, a robotic manipulator on a mobile platform. Our machine differs from classic mobile manipulators because it uses a 6-DOF PKM as a manipulator and a six-parallel-legged robot as a mobile platform. The upper PKM features high stiffness and high precision, which are crucial for machining tasks. Meanwhile, the lower legged robot provides a system with higher mobility and better adaptability for locomotion tasks compared with wheeled or tracked vehicles. Moreover, the parallel kinematic leg architecture allows the lower legged robot to overcome the disadvantages of low payload and low rigidity, which are common in most legged robots. In contrast to WalkingHex, our proposed walking machine tool has a complete PKM module; hence, the kinematic calibration process before every machining task is unnecessary. In addition, each leg of the lower legged robot is actuated by three ball screws, thereby providing the leg with high payload and high accuracy during the walking phase.

The rest of this paper is organized as follows. The overall description of the walking machine tool is presented in Section 2. Kinematic models of the leg, body, and head are described, and the workspace of the three components is analyzed in Section 3. A hierarchical motion planning scheme with simulations is proposed in Section 4, and two experiments are performed in Section 5. The first experiment measures the repeatability of the three motion layers, and the second experiment demonstrates an application scenario combining the three motion layers. Finally, conclusions are provided in Section 6.

2 System overview

2.1 Design concept

The main design objective of the six-legged walking machine tool is to provide high accuracy for a PKM tool and maintain the locomotivity of a legged robot. Mobile processing applications require mobile machine tools with high precision, high rigidity, and high payload. Our laboratory designed a six-legged walking robot with a three-limb parallel mechanism for its leg design. The novel legs allow the robot to carry a payload of 200 kg [22]. A

late-generation version of this robot was utilized to perform low-precision tasks, such as opening doors [23] and turning valves [24]. However, the body motion accuracy of the legged robot failed to satisfy machining requirements. Therefore, a manipulator is mounted on the body of the six-legged robot to conduct high-precision tasks.

For versatility, the manipulator is expected to have six DOFs. In addition, parallel kinematic manipulators are preferred owing to their superiority in terms of precision, rigidity, and payload compared with serial manipulators. The most common mechanisms that meet the above conditions are the 6-universal-prismatic-spherical (6-UPS), which is known as the Stewart platform, and the 6-prismatic-universal-spherical (6-PUS), which is also called the Hexaslide [25]. The latter has an advantage in small moving inertia and fast dynamic response, because its actuators are all mounted on a fixed base. Moreover, fixed mounting type actuators are convenient for cable routing. Therefore, a 6-PUS parallel mechanism is chosen to design the mobile manipulator mounted on the body.

2.2 Mechanical description

A physical prototype of the six-legged mobile machine tool is shown in Fig. 1. From a topology perspective, the mobile machine tool consists of seven parallel mechanisms, namely, six legs and a PKM head. These mechanisms are mounted on a single base, that is, the body. The overall dimension of the walking machine tool is shown in Fig. 2. The walking machine tool is 1685 mm wide, 1295 mm long, and 1362 mm high.

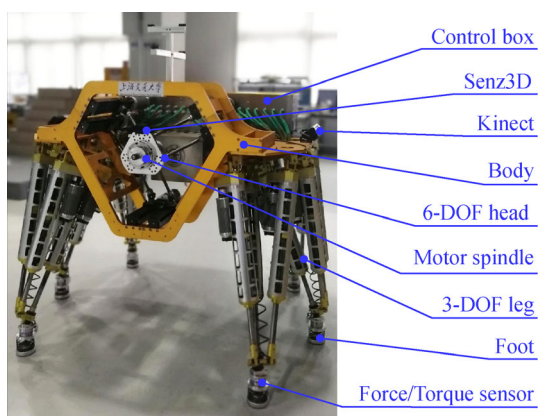


Fig. 1 Physical prototype of the six-legged walking machine tool.

1) *Leg*. A 1-UP and 2-UPS parallel mechanism is employed for the leg design. In this notation, U represents a passive universal joint, P denotes an active prismatic joint, and S stands for a passive spherical joint. The active prismatic joint is embodied by an originally designed

linear actuator driven by a direct current (DC) servo motor through a gear box, a synchronous belt, and a ball screw. The three chains are connected to a triangle base plate with universal joints. A small triangle structural component, which is considered as the ankle of the leg, is fixed at the end of the UP chain piston rod. The piston rods of the UPS chains are connected to the ankle by spherical joints. A 6-DOF force/torque sensor is mounted under the ankle, and another passive spherical joint connecting the foot is mounted on the other side of the sensor.

2) *Body*. The robot body consists of two aluminum plates connected by steel ribs. The body is designed to be as compact as possible while providing adequate mounting space for the legs and PKM head. The six legs are symmetrically arranged under the body. The PKM head is mounted on the front of the body, and the control box and lithium batteries are mounted on the back, thereby making the weight distributed in equilibrium. The structural frame of the PKM head can increase the rigidity of the body. The control box contains the controllers and servo drives.

3) *Head*. The architecture of the robot head is a 6-PUS parallel mechanism. Six linear actuators are mounted on a hexagonal prismatic frame. The slider on each linear actuator is driven by a DC motor through a ball screw. A moving platform housing an electric spindle is connected to all the sliders by six links. Each link has two universal joints on both sides. Moreover, each link consists of two coaxial rods with a revolute joint in between. The axis of revolution goes through the universal joint centers. For brevity, the function of one universal joint and the revolute joint is equivalent to that of a spherical joint.

2.3 Control architecture

The control architecture of the walking machine tool is illustrated in Fig. 3. It consists of two controllers: (a) The locomotion controller running a self-developed legged robot control program on top of Linux with a real-time infrastructure named Xenomai, controlling 18 DC motors of the legged mobile platform; and (b) the manipulation controller running Beckhoff TwinCAT3 on top of Windows 10, controlling six DC motors of the PKM head. All the servo drives are connected to the controllers through the EtherCAT real-time network. The locomotion controller is the main controller, receiving commands from the remote terminal and giving commands to the manipulation controller. Two Microsoft Kinect vision sensors are mounted on the left and right sides of the body and connected to the locomotion controller through a USB interface. The sensors are utilized for autonomous obstacle avoidance. A Creative BlasterX Sens3D depth-sensing camera is mounted on the spindle platform and connected to the manipulation controller. The camera is employed to locate a workpiece with respect to the mobile machine tool. The camera also provides an image signal for the visual servo processing task.

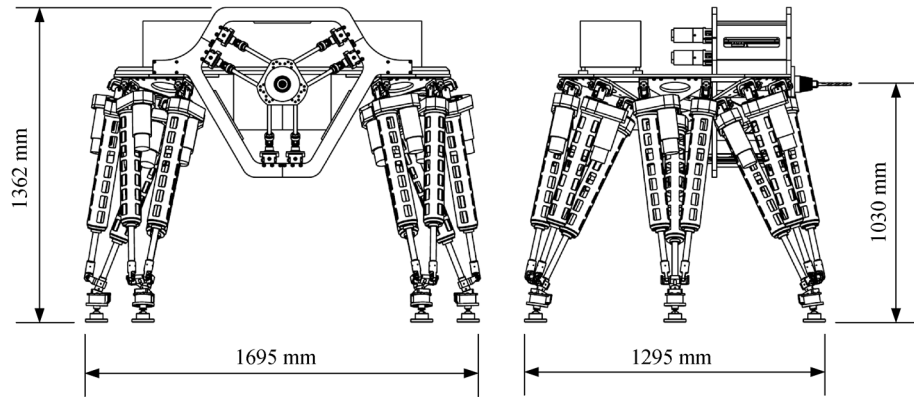


Fig. 2 Dimensions of the front and side views of the walking machine tool.

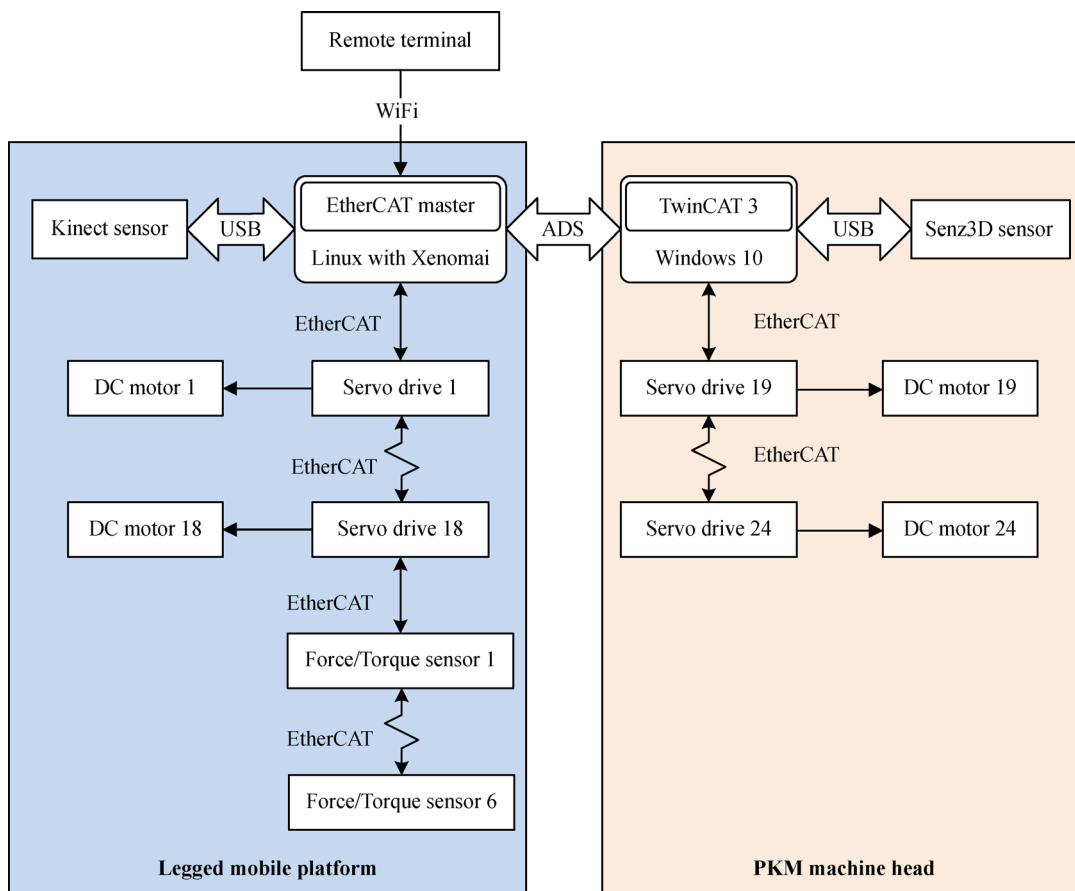


Fig. 3 Control architecture of the walking machine tool.

2.4 Motion layers

A hierarchical motion planning scheme is proposed to take advantage of the large workspace of the legged mobile platform and the high precision of the PKM head, as shown in Fig. 4. The walking machine tool involves 24 actuations, which presents a motion planning challenge. Hence, we divide the motion of the system into three layers based on the moving subjects. The leg motion layer is utilized to

execute the walking task and to lead the machine tool to the target position. This layer has the largest working range but the lowest precision. The body motion layer is used to adjust the pose of the body, bring the PKM head near a workpiece, or expand the working range of the PKM head. This layer has an intermediate working range and intermediate precision. The head motion layer is employed to execute the machining task. This layer has the smallest working range but the highest precision.

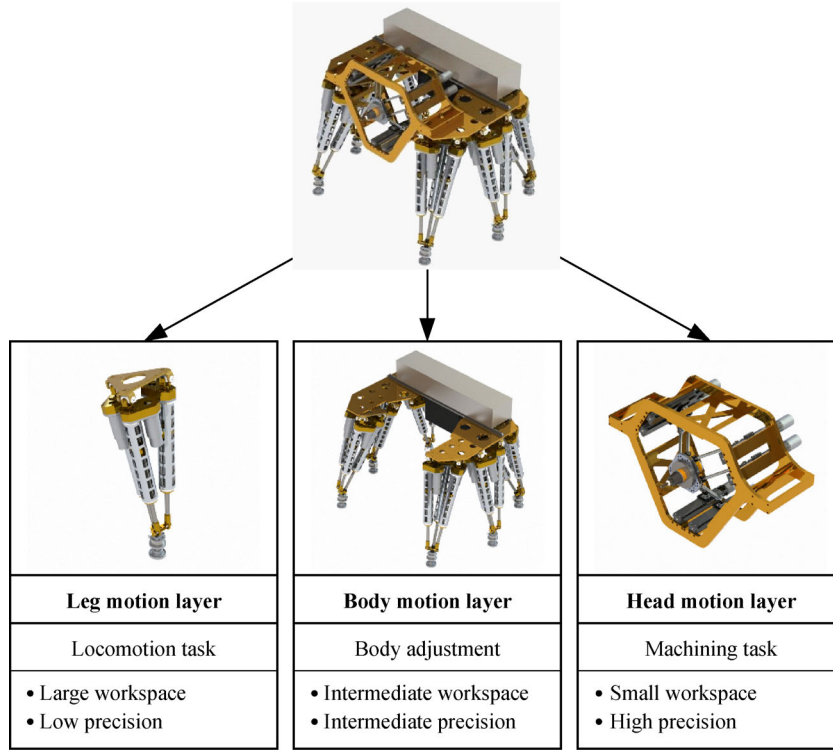


Fig. 4 Three motion layers of the walking machine tool.

3 Kinematic model and workspace analysis

3.1 Inverse kinematics

First, we need to derive the inverse kinematic solution of a single leg. The schematic diagram of the leg mechanism is shown in Fig. 5. In a coordinate frame, the red, green, and blue arrows indicate the x , y , and z axes, respectively. This notation is also used in other figures in this paper. The centers of the universal joints and spherical joints are denoted by U_{ji} and S_{ji} , respectively, where the subscript i ($i = 1, 2, \dots, 6$) is the leg index, and the subscript j is the chain index ($j = 1$ for the \underline{UP} chain, and $j = 2$ and 3 for the \underline{UPS} chains). The foot is connected to the \underline{UP} chain with another passive spherical joint whose center is denoted by S_{fi} . S_{fi} is also used as the end-effector center point for the motion planning of the leg mechanism.

A reference frame $\{H_i\}$, which stands for the hip frame, is fixed to the triangle base plate, while the origin O_{Hi} is coincident with U_{1i} . Its x axis is perpendicular to the plane $U_{1i}U_{2i}U_{3i}$, while its z axis is parallel to the vector $\overrightarrow{U_{3i}U_{2i}}$. A moving frame $\{A_i\}$, which represents the ankle frame, is attached to the piston rod of the \underline{UP} chain. Its x axis is coincident with the prismatic joint axis of the \underline{UP} chain, which goes through O_{Hi} . Its yz plane goes through S_{2i} , and its z axis is parallel to the vector $\overrightarrow{S_{3i}S_{2i}}$. Thus, its origin O_{Ai} can be derived. The joint coordinates of the parallel leg

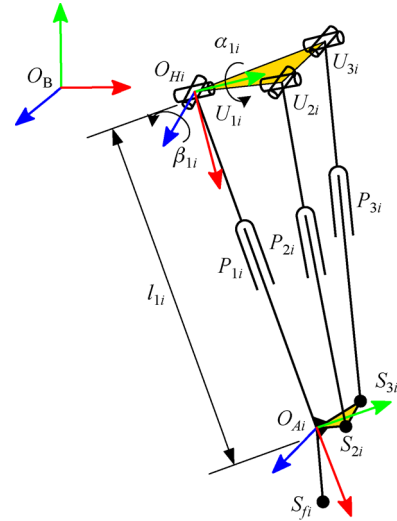


Fig. 5 Schematic diagram of the parallel leg mechanism.

mechanism are the lengths of each chain. The specific definitions are shown in the following equations:

$$l_{1i} = \|U_{1i}O_{Ai}\|, \quad (1)$$

$$l_{2i} = \|U_{2i}S_{2i}\|, \quad (2)$$

$$l_{3i} = \|U_{3i}S_{3i}\|. \quad (3)$$

The inverse kinematics of the 1-UP and 2-UPS parallel mechanism is to calculate the joint coordinates given the Cartesian coordinates of S_{fi} with respect to the hip frame $\{H_i\}$. It can be derived based on the vector loop method. The vector loop $O_{Hi}O_{Ai}S_{fi}O_{Hi}$ is considered to calculate the generalized coordinates of the UP chain:

$${}^{Hi}\mathbf{S}_{fi} = {}^{Hi}\mathbf{T}_{Ai} \cdot {}^{Ai}\mathbf{S}_{fi}, \quad (4)$$

where ${}^{Hi}\mathbf{S}_{fi} = [x_i \ y_i \ z_i]^T$ are the input variables of the inverse kinematics, and ${}^{Ai}\mathbf{S}_{fi} = [S_{fxi} \ S_{fyi} \ S_{fzi}]^T$ are given as the kinematic parameters. In this notation, the pre-superscript H_i in the symbol ${}^{Hi}\mathbf{S}_{fi}$ indicates that the vector is expressed relative to the frame $\{H_i\}$, and so on. And the homogeneous transformation matrix ${}^{Hi}\mathbf{T}_{Ai}$ serves as the description of frame $\{A_i\}$ relative to $\{H_i\}$. According to the definition of the ankle frame $\{A_i\}$ and UP chain structure, ${}^{Hi}\mathbf{T}_{Ai}$ is determined by the two rotation angles of the universal joint and the displacement of the prismatic joint:

$${}^{Hi}\mathbf{T}_{Ai} = \begin{bmatrix} c\alpha_{1i}c\beta_{1i} & -c\alpha_{1i}s\beta_{1i} & s\alpha_{1i} & l_{1i}c\alpha_{1i}c\beta_{1i} \\ s\beta_{1i} & c\beta_{1i} & 0 & l_{1i}s\beta_{1i} \\ -s\alpha_{1i}c\beta_{1i} & s\alpha_{1i}s\beta_{1i} & c\alpha_{1i} & -l_{1i}s\alpha_{1i}c\beta_{1i} \\ 0 & 0 & 0 & 1 \end{bmatrix}, \quad (5)$$

where α_{1i} and β_{1i} are the first and second rotation angle of the universal joint in the UP chain, respectively, and $s\alpha_{1i}$ is the shorthand for $\sin\alpha_{1i}$, $c\alpha_{1i}$ is the shorthand for $\cos\alpha_{1i}$, and so on.

By combining Eqs. (4) and (5), the generalized coordinates of the UP chain can be calculated as follows:

$$l_{1i} = \sqrt{x_i^2 + y_i^2 + z_i^2 - S_{fyi}^2 - S_{fzi}^2 - S_{fxi}}, \quad (6)$$

$$\beta_{1i} = \arcsin \frac{y_i}{\sqrt{(l_{1i} + S_{fxi})^2 + S_{fyi}^2}} - \arcsin \frac{S_{fxi}}{\sqrt{(l_{1i} + S_{fxi})^2 + S_{fyi}^2}}, \quad (7)$$

$$\alpha_{1i} = \arctan \frac{S_{fxi}x_i - [(l_{1i} + S_{fxi})c\beta_{1i} - S_{fyi}c\beta_{1i}]z_i}{[(l_{1i} + S_{fxi})c\beta_{1i} - S_{fyi}s\beta_{1i}]x_i + S_{fzi}z_i}. \quad (8)$$

Hence, ${}^{Hi}\mathbf{T}_{Ai}$ is obtained by substituting Eqs. (6)–(8) into Eq. (5). The lengths of UPS chains l_{2i} and l_{3i} can be calculated as follows:

$$l_{2i} = \|{}^{Hi}\mathbf{T}_{Ai} \cdot {}^{Ai}\mathbf{S}_{2i} - {}^{Hi}\mathbf{U}_{2i}\|, \quad (9)$$

$$l_{3i} = \|{}^{Hi}\mathbf{T}_{Ai} \cdot {}^{Ai}\mathbf{S}_{3i} - {}^{Hi}\mathbf{U}_{3i}\|, \quad (10)$$

where ${}^{Hi}\mathbf{U}_{2i}$ and ${}^{Hi}\mathbf{U}_{3i}$ respectively stand for the positions of U_{2i} and U_{3i} with respect to the frame $\{H_i\}$.

Thus, the relationship between ${}^{Hi}\mathbf{S}_{fi}$ and the joint coordinates is derived:

$$\mathbf{q}_i = [l_{1i} \ l_{2i} \ l_{3i}]^T. \quad (11)$$

Next, we need to express the leg kinematic model in the body frame. All six legs are symmetrically distributed around the body frame $\{B\}$, as shown in Fig. 6. The base plate of each leg is fixed under the body structure; hence, the pose of frame $\{H_i\}$ relative to $\{B\}$ is constant. Generally, motion planning for legged robots is implemented in two ways, that is, either planning foot-tip positions relative to the body frame or planning the body pose and foot-tip positions simultaneously with respect to the ground frame $\{G\}$. The second method can be converted to the first method by applying a matrix transformation:

$${}^B\mathbf{S}_{fi} = {}^G\mathbf{T}^{-1} \cdot {}^G\mathbf{S}_{fi}, \quad (12)$$

where ${}^G\mathbf{T}$ is the homogeneous transformation matrix representing the body pose with respect to frame $\{G\}$, ${}^B\mathbf{S}_{fi}$ and ${}^G\mathbf{S}_{fi}$ respectively denote the positions of foot-tip S_{fi} with respect to frame $\{B\}$ and frame $\{G\}$. Thus, we need to express the inverse kinematics of the leg mechanism in the body frame.

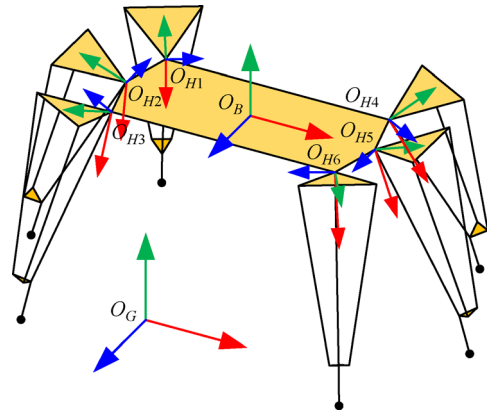


Fig. 6 Definition of coordinate systems in the legged mobile platform.

The description of the i th hip frame $\{H_i\}$ with respect to the body frame $\{B\}$ is expressed as follows:

$${}^B\mathbf{T}_{Hi} = \begin{bmatrix} {}^B\mathbf{R}_{Hi} & {}^B\mathbf{p}_{Hi} \\ \mathbf{0} & 1 \end{bmatrix}, \quad (13)$$

where ${}^B\mathbf{p}_{Hi} = [H_{xi} \ H_{yi} \ H_{zi}]^T$ is the origin position of $\{H_i\}$ with respect to $\{B\}$, and the rotation matrix ${}^B\mathbf{R}_{Hi}$ is expressed by ZXZ-Euler angles $[\varphi_i \ \theta_i \ \psi_i]^T$.

$${}^B_{Hi}R = R_z(\varphi_i)R_x(\theta_i)R_z(\psi_i), \quad (14)$$

where $R_z(\varphi_i)$ is a rotation matrix that represents a rotation about z axis by φ_i degrees, and so on.

While planning the trajectory of the legged mobile platform, the body pose and all foot-tip locations with respect to the ground frame are given simultaneously.

$${}^{Hi}S_{fi} = {}^B_{Hi}T^{-1} \cdot {}^B S_{fi}. \quad (15)$$

Hence, we can use Eqs. (6), (9), and (10) for each leg to calculate all 18 joint variables in the legged mobile platform.

Finally, we derive the inverse kinematics of the 6-PUS machine head. The mechanism schematic is shown in Fig. 7. A_k and B_k represent the rotation centers of the spherical joint and the universal joint in the k th chain, respectively; B_{k0} is the initial position of B_k when the actuators are on their home position; and e_k represents the unit direction vector of the k th prismatic joint. Therefore, the input variables are the distances between B_k and B_{k0} . A moving frame $\{P\}$ is attached to the spindle platform. Its origin is located in the center of the hexagon $A_1A_2A_3A_4A_5A_6$. Its z axis is perpendicular to the hexagon plane, while its x axis is parallel to the vector $\overrightarrow{A_2A_1}$. Its y axis is derived by the right-hand rule. A reference frame $\{M\}$ is attached to the machine casing and coincident with $\{P\}$ when all the prismatic joints are in their home position.

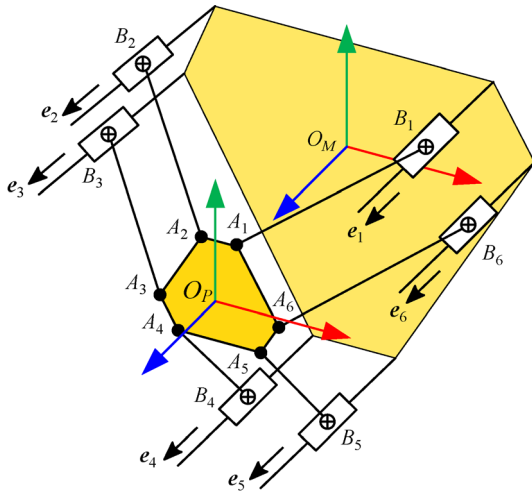


Fig. 7 Schematic diagram of the PKM head.

For the k th kinematic chain, according to the vector loop method, we have

$${}^M P_P + {}^M_P R \cdot {}^P a_k = {}^M b_{0k} + q_k e_k + {}^M l_k, \quad (16)$$

where ${}^M P_P$ stands for the origin location vector of $\{P\}$ with respect to $\{M\}$, ${}^M_P R$ is a rotation matrix describing

$\{P\}$ relative to $\{M\}$, ${}^P a_k$ stands for the location of the k th universal joint center S_k with respect to the moving platform frame $\{P\}$, ${}^M b_{0k}$ represents the location of U_{0k} with respect to the machine frame $\{M\}$, $l_k = \overrightarrow{B_k A_k}$, and q_k is the k th joint coordinate.

For brevity, we define

$$h_k = {}^M P_P + {}^M_P R \cdot {}^P a_k - {}^M b_{0k}. \quad (17)$$

Hence,

$$l_k = h_k - q_k e_k. \quad (18)$$

By squaring both sides of the equation above, we obtain

$$L_k^2 = h_k^T h_k - 2q_k h_k^T e_k + q_k^2. \quad (19)$$

Two solutions exist for a quadratic equation, but only one of the solutions satisfies the continuity condition considering the initial position of the slider.

$$q_k = h_k^T e_k - \sqrt{(h_k^T e_k)^2 - h_k^T h_k + L_k^2}. \quad (20)$$

The joint coordinates are calculated by applying Eq. (20) to all six chains.

$$q = [q_1 \quad q_2 \quad \cdots \quad q_6]^T. \quad (21)$$

3.2 Workspace analysis

In this section, we analyze the workspace of three different components, including a single leg, the body, and the PKM head.

The workspace of the leg mechanism can be obtained with the discretization method. The workspace of a single leg is searched by discretizing the Cartesian coordinates of the foot-tip, applying inverse kinematics, and checking joint variable limits, as follows:

$$\begin{cases} l_{j\min} \leq l_j \leq l_{j\max}, \\ \cos\alpha_1 \cos\beta_1 \leq \cos\theta_m, \end{cases} \quad j = 1, 2, 3, \quad (22)$$

where θ_m is the maximum tilt angle of the universal joint in the UP chain.

The workspace boundary with respect to the body frame is shown in Fig. 8(a). A red cylinder is drawn within the workspace to visually represent the range of the foot-tip motion when the mobile platform walks. The cylinder's diameter represents the maximum walking step length, and its height indicates the corresponding step height. The maximum height of the cylinder is 0.12 m when its diameter is set to 0.8 m. When the diameter is reduced to 0.4 m, the height can reach up to 0.25 m. The cylinder is meaningful for choosing the proper walking step parameters.

With all the feet fixed on the ground, the body can function as a redundantly actuated 6-DOF platform. The

body workspace can be determined by discretizing the body pose parameters and checking the boundary conditions with Eq. (22) for all six legs.

The PKM head workspace can also be calculated using the same methods. The constraint conditions are the six joint variable range limits.

$$q_{k\min} \leq q_k \leq q_{k\max}, k = 1, 2, \dots, 6. \quad (23)$$

The translational workspace of the body and PKM head is shown in Figs. 8(b) and 8(c), respectively. We draw a maximal cube within each working envelope. The cubes are utilized to generate testing poses for the performance evaluation according to the *ISO 9283:1998 Manipulating Industrial Robots—Performance Criteria and Related Test Methods* standards [26]. Furthermore, the cubes can intuitively represent the size of the workspace. The cube in the body workspace has an edge length of 0.25 m, whereas the cube in the head workspace has an edge length of 0.075 m. Obviously, the working range of the PKM head is much smaller than that of the body.

4 Hierarchical motion planning and simulation

4.1 General workflow

A general workflow combing the three motion layers to perform a processing task is shown in Fig. 9. First, the robot is navigated to a workpiece from an initial position using the bottom motion layer. Second, the body adjusts its pose to locate the PKM head in a proper position using the middle motion layer. Finally, the PKM head deals with the machining tasks using the top motion layer.

4.2 Leg motion layer

Various walking gaits can be applied to a six-legged robot. Among them, the tripod gait is the most efficient for planning. The legs are numbered, as shown in Fig. 6. The first, third, and fifth legs are divided into the first group, and the rest of the legs are divided into the second group. When one group of legs is swinging, the other group of

legs stands on the ground supporting the body. Using the tripod gait, the robot can walk in any direction and turn on the horizontal plane.

A typical forward-walking gait with two cycles is demonstrated in Fig. 10, where d and h stand for the step length and step height, respectively, and T represents a walking cycle. Each cycle consists of two steps, and each step takes a half cycle. According to Figs. 10(a) and 10(b), during the first half cycle, the first group of legs swings forward with a distance of $0.5d$, while the second group of legs stands on the ground. The swing trajectory of each foot with respect to the ground frame is a semi-ellipse curve. Similarly, in the final half cycle, the second group of legs steps forward $0.5d$. During the period in between, each group swings alternately every half cycle with a distance of d . Correspondingly, the body motion can be divided into three phases, namely, the accelerated motion phase, the uniform motion phase, and the decelerated motion phase. From 0 to $0.5T$, the body accelerates to the target speed d/T and maintains the speed during the next cycle. In the final half cycle, that is, from $1.5T$ to $2T$, the body decelerates from the velocity to stop. The feet trajectories with respect to the body frame are shown in Fig. 10(c). This walking gait can be generalized easily to additional cycles. The number of walking cycles is denoted by n . Leg motions between $0.5T$ and $1.5T$ are repeated $n-1$ times, and the overall walking distance is $(n-0.5)d$.

A simulation intuitively demonstrates the walking motion of the mobile machine tool, as shown in Fig. 11. The captures show the leg configurations every half cycle.

4.3 Body motion layer

As analyzed in Section 3.2, the workspace of the PKM head is extremely limited. Therefore, we need to use the body motion layer to extend the working range of the tool center point (TCP). This layer is employed when all six feet are standing on the ground, thereby making it more accurate than the walking motion. Support from multiple legs also leads to higher stiffness compared with locomotion via alternating legs. The purpose of this level is to convey the PKM head to its preferable posture relative to the processing area in a large workpiece. As illustrated in

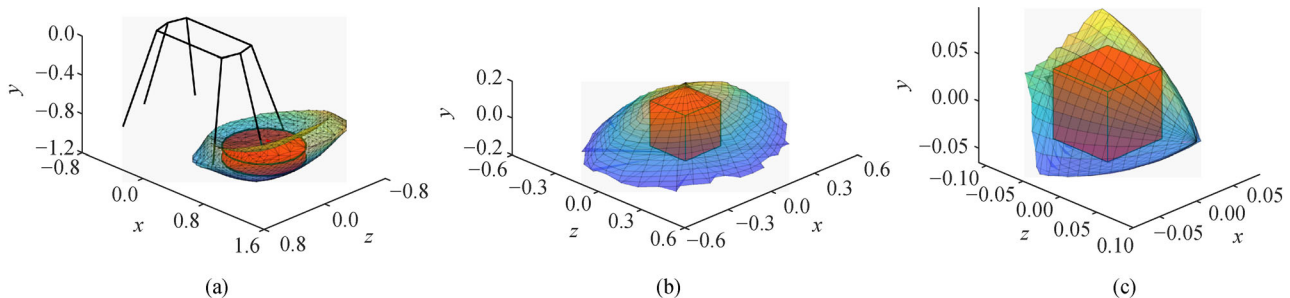


Fig. 8 Workspace of different components of the walking machine tool. (a) Leg; (b) body; (c) head.

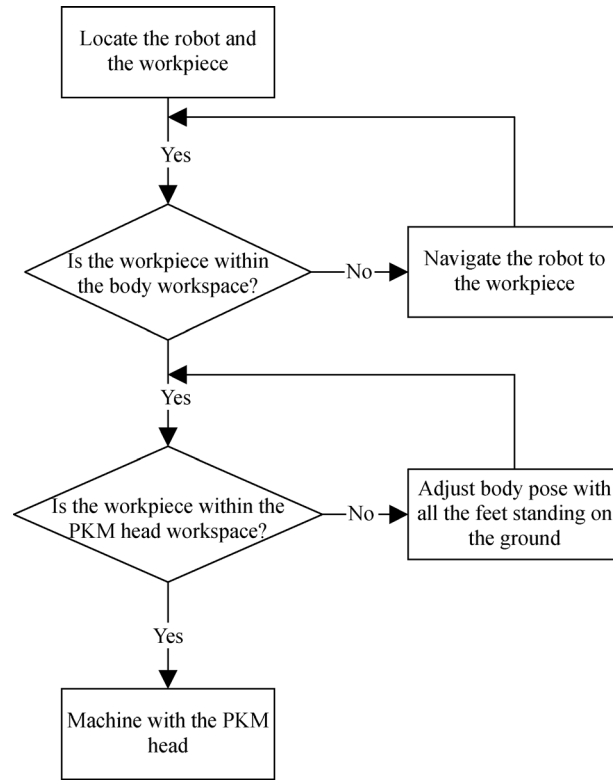


Fig. 9 Workflow of the walking machine tool for performing mobile machining tasks.

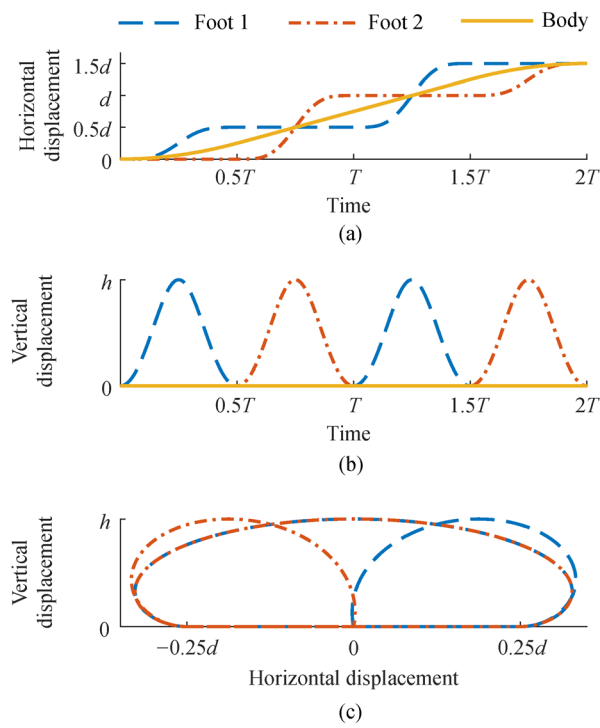


Fig. 10 Feet trajectories in two walking cycles. (a) Horizontal and (b) vertical displacements of feet and body; (c) feet trajectories with respect to the body frame.

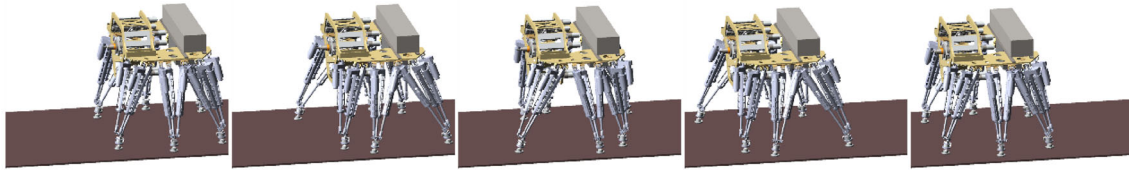


Fig. 11 Snapshots of the walking simulation.

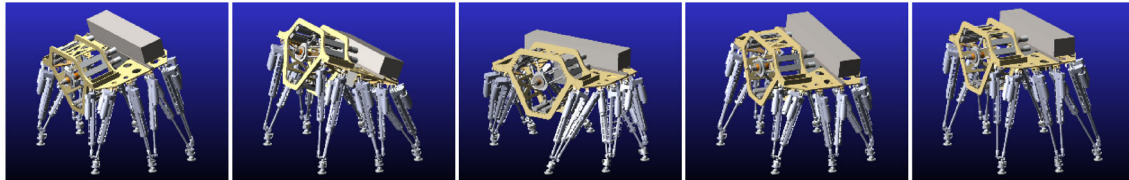


Fig. 12 Snapshots of the body twisting simulation.

Fig. 12, multiple support legs enable the robot body to engage in flexible behaviors.

The body pose adjustment uses point-to-point motion in a six-dimensional space. We interpolate the pose parameters with cubic splines, with position and velocity values specified at the beginning and ending moments.

4.4 Head motion layer

The head motion presents the highest precision of the system, thereby satisfying industrial requirements. The PKM head is designed to include all six spatial DOFs (Fig. 13). Hence, it can adapt its pose to curved working surfaces. In the machining process, the first step is to construct the workpiece coordinate frame $\{W\}$ by scanning the workpiece feature using the vision sensor on the PKM head or an external positioning device. In addition, ${}^M_W\mathbf{T}$, which is the relationship between the machine frame $\{M\}$ and the workpiece frame $\{W\}$, is determined. Besides, the TCP position offset with respect to the spindle platform frame $\{P\}$ must be measured to obtain the pose of the tool frame $\{T\}$ relative to $\{P\}$, which is denoted by ${}^P_T\mathbf{T}$. The machining process is performed by planning the motion of the tool frame $\{T\}$ relative to the workpiece frame $\{W\}$, namely, ${}^W_T\mathbf{T}$. The path of ${}^W_T\mathbf{T}$ can be preprogrammed tool paths or sensor-based online-generated paths. ${}^W_T\mathbf{T}$ can be expressed as a

product of transformations in two different ways, which constructs a transform equation:

$${}^M_P\mathbf{T} \cdot {}^P_T\mathbf{T} = {}^M_W\mathbf{T} \cdot {}^W_T\mathbf{T}. \quad (24)$$

Thus, the path of ${}^W_T\mathbf{T}$ can be transferred to the path of ${}^M_P\mathbf{T}$, that is, the relative pose between the spindle platform frame and the machine frame.

$${}^M_T = {}^M_W\mathbf{T} \cdot {}^W_T\mathbf{T} \cdot {}^P_T\mathbf{T}^{-1}. \quad (25)$$

The head motion trajectories are generated by combining Eq. (25) with the inverse kinematics of the PKM head.

5 Experiment

5.1 Repeatability test

The repeatability of the three motion layers was tested based on ISO 9283 standards [26]. A Leica AT960 laser tracker (Fig. 14(a)) was used as the measurement equipment. The spindle was removed from the PKM head and replaced with a calibration plate with three magnetic nests to hold the spherically mounted retro-reflector (SMR; Fig. 14(b)).

The repeatability test (Fig. 14) of the leg motion layer was performed by commanding the legged mobile platform to walk forward and backward for 30 cycles and

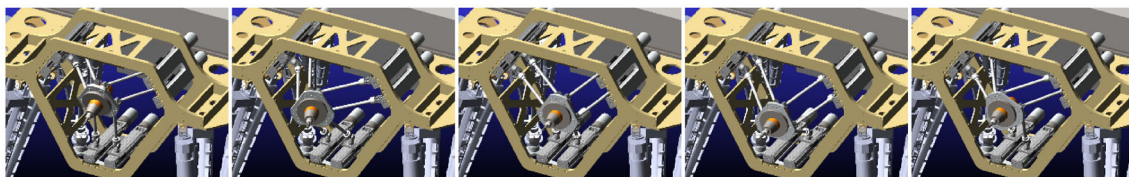


Fig. 13 Snapshots of the PKM head twisting simulation.

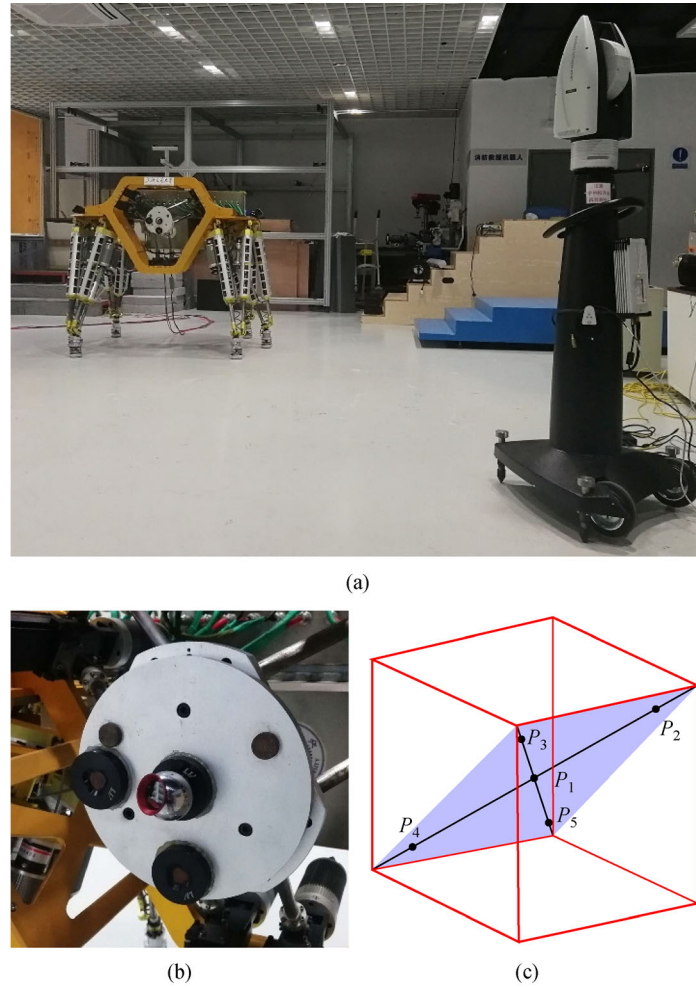


Fig. 14 Experiment setup of the repeatability test. (a) Overall setup; (b) SMR holders on the moving platform; (c) commanded poses.

using a laser tracker to measure the body displacements. The PKM head was disabled and kept still during the walking motion. Therefore, the displacement of the SMR on the head could represent the body displacement. The repeatability of the walking motion was affected by not only the inherent accuracy of the legged robot but also the roughness of the ground. The positioning error of the walking motion accumulated as the cycle increased. Thus,

we used the walking distance error to represent the walking motion repeatability. The test was performed with different walking steps from one to three, and the result is shown in Fig. 15(a).

The repeatability test of the body motion was performed by commanding the body to move to five target poses for 30 cycles. As shown in Fig. 14(c), the commanded poses were arranged in the largest available cube at the center of

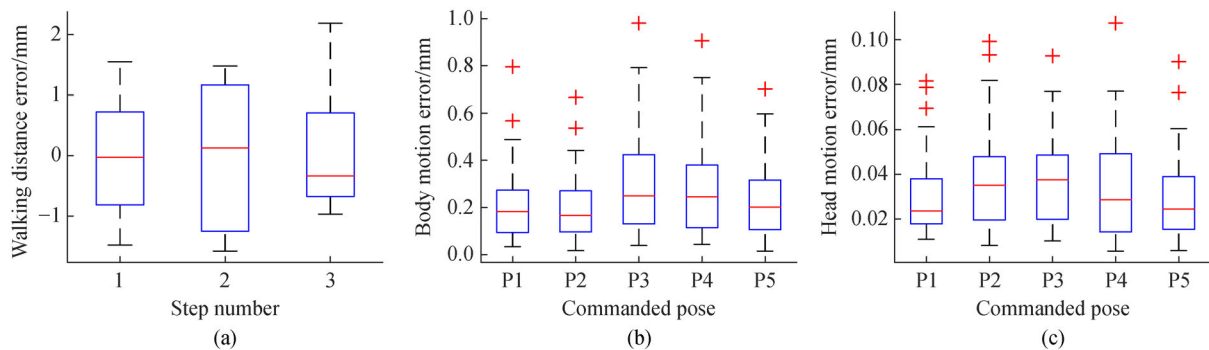


Fig. 15 Repeatability test results of different motion layers. (a) Walking; (b) body motion; (c) head motion.

the working volume and offset by 10% of the diagonal distance. The head motion repeatability was tested in the same way for 30 cycles, with all leg actuators locked. The pose repeatability is defined as follows:

$$RP_l = \bar{l} + 3S_l, \quad (26)$$

$$\bar{l} = \frac{1}{n} \sum_{j=1}^n l_j, \quad (27)$$

$$l_i = \sqrt{(x_i - \bar{x})^2 + (y_i - \bar{y})^2 + (z_i - \bar{z})^2}, \quad (28)$$

$$S_l = \sqrt{\frac{\sum_{j=1}^n (l_j - \bar{l})^2}{n-1}}, \quad (29)$$

where RP_l is the pose repeatability, \bar{l} and S_l are the mean value and standard deviation of the position error, respectively, and l_j is the distance between the j th measured coordinates and the mean values. The pose repeatability of each target pose was calculated by applying Eqs. (26)–(29) to the measured poses. The maximum value of the five-pose repeatability was taken as the motion repeatability.

The results are presented in Fig. 15 in term of boxplots. The repeatability of the head motion was 0.11 mm and that of the body motion was 1.0 mm. This finding proved that the head motion was more precise than the body motion. The walking distance repeatability was 3.4 mm; hence, the walking motion demonstrated the lowest precision.

5.2 Application scenario

An *in-situ* operation experiment was conducted to demonstrate the three-level motions of the walking machine tool, as shown in Fig. 16. The workpiece was an aluminum plate mounted on a steel frame, and the processing task was to drill a hole in it.

First, the robot was navigated to the workpiece from an initial position. The kinetic sensor mounted on the body

detected a 250 mm-high and a 100 mm-wide obstacle lying on the walking path. The robot adjusted its walking gait to step over the obstacle. It lifted its body to make full use of the leg workspace and walk with a 270 mm step height. After stepping over the obstacle and approaching the target workpiece, the robot stopped in front of it. Next, the depth-sensing camera mounted on the spindle platform scanned the workpiece and fitted the generated point cloud to construct the workpiece coordinate system $\{W\}$. Based on the relative pose W_T , the robot adjusted its body pose to move closer to the workpiece and bring the working region within the workspace of the PKM head. In the top layer motion phase, the legged mobile platform stood still, and the PKM head adjusted the pose of the spindle platform to keep the spindle axis perpendicular to the working surface. Subsequently, the spindle started to turn, and the feed motion along the tool axis was performed by the PKM head. Finally, a hole was successfully drilled at the desired location.

6 Conclusions

A novel six-legged walking machine tool consisting of a six-parallel-legged walking robot and a 6-DOF PKM tool is proposed for the first time. The walking machine tool integrates high mobility, high precision, and terrain adaptability to address the requirements of *in-situ* maintenance for large parts. A 1-UP and 2-UPS parallel mechanism is chosen for the leg design, and a symmetric 6-PUS parallel mechanism is selected for the machine head design. Moreover, the kinematic model and control architecture of the system are discussed. A hierarchical motion planning scheme divides the system motion into three layers, that is, the leg motion layer for locomotion, the body motion layer for adjustment, and the head motion layer for machining.

In addition, the workspace of the three motion layers is analyzed. The leg workspace envelops a cylinder with a diameter of 0.8 m and a height of 0.12 m or a cylinder with a diameter of 0.4 m and a height of 0.25 m, thereby allowing the robot to walk with a large step length and a

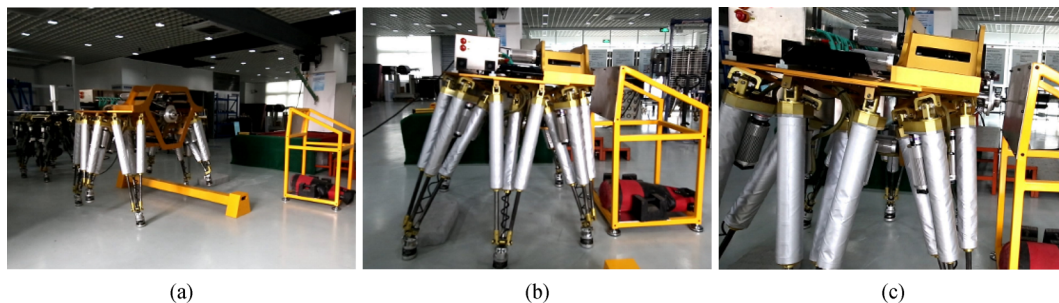


Fig. 16 Multi tasks in an application scenario. (a) Stepping over an obstacle; (b) adjusting body pose; (c) drilling a hole on the workpiece.

large step height. The workspace of the body and head can envelop a cube with a side length of 0.25 and 0.075 m, respectively. Motion simulations show how these motion layers work. In addition, their repeatability is tested through experiments. The repeatability of the head motion, body motion, and walking distance is 0.11, 1.0, and 3.4 mm, respectively. The results prove the rationality of the task division for the three motion layers.

Finally, a comprehensive experiment that requires the robot to step over a 250 mm-high obstacle and perform an autonomous drilling task is conducted to demonstrate the workflow of the system and prove the validity of the hierarchical motion planning scheme. The walking machine tool presented in this paper will hopefully become an intelligent and multifunctional solution for *in-situ* processing of large parts.

Acknowledgements This work was funded by the National Natural Science Foundation of China (Grant No. U1613208), the National Key Research and Development Plan of China (Grant No. 2017YFE0112200), and the European Union's Horizon 2020 Research and Innovation Programme under the Marie Skłodowska-Curie grant agreement No. 734575.

Electronic Supplementary Material The supplementary material can be found in the online version of this article (<https://doi.org/10.1007/s11465-020-0594-2>) and is accessible to authorized users.

Open Access This article is licensed under a Creative Commons Attribution 4.0 International License, which permits use, sharing, adaptation, distribution and reproduction in any medium or format, as long as you give appropriate credit to the original author(s) and the source, provide a link to the Creative Commons licence, and indicate if changes were made.

The images or other third party material in this article are included in the article's Creative Commons licence, unless indicated otherwise in a credit line to the material. If material is not included in the article's Creative Commons licence and your intended use is not permitted by statutory regulation or exceeds the permitted use, you will need to obtain permission directly from the copyright holder.

To view a copy of this licence, visit <http://creativecommons.org/licenses/by/4.0/>.

References

- Uriarte L, Zatarain M, Axinte D, et al. Machine tools for large parts. *CIRP Annals*, 2013, 62(2): 731–750
- Bostelman R, Hong T, Marvel J. Survey of research for performance measurement of mobile manipulators. *Journal of Research of the National Institute of Standards and Technology*, 2016, 121: 342–366
- Suárez R, Palomo-Avellaneda L, Martínez J, et al. Development of a dexterous dual-arm omnidirectional mobile manipulator. *IFAC-PapersOnLine*, 2018, 51(22): 126–131
- Olazagoitia J L, Wyatt S. New PKM Tricept T9000 and Its Application to Flexible Manufacturing at Aerospace Industry. *SAE Technical Paper 2007-01-3820*, 2007
- Law M, Rentzsch H, Ihlenfeldt S. Development of a dynamic substructuring framework to facilitate *in situ* machining solutions using mobile machine tools. *Procedia Manufacturing*, 2015, 1: 756–767
- Hazel B, Côté J, Laroche Y, et al. *In-situ* robotic interventions in hydraulic turbines. In: *Proceedings of the 2010 1st International Conference on Applied Robotics for the Power Industry*. Montreal: IEEE, 2010, 11637498
- Hazel B, Boudreault E, Côté J, et al. Robotic post-weld heat treatment for in situ repair of stainless steel turbine runners. In: *Proceedings of the 2014 3rd International Conference on Applied Robotics for the Power Industry*. Foz do Iguassu: IEEE, 2014, 14903693
- Collado V, Arana J, Saenz A. A Crawling Portable Robot for Drilling Operations in Large Air Frame Components. *SAE Technical Paper 2005-01-3337*, 2005
- Marguet B, Cibiel C, De Francisco Ó, et al. Crawler Robots for Drilling and Fastener Installation: An Innovative Breakthrough in Aerospace Automation. *SAE Technical Paper 2008-01-2292*, 2008
- Pessi P, Wu H, Handroos H, et al. A mobile robot with parallel kinematics to meet the requirements for assembling and machining the ITER vacuum vessel. *Fusion Engineering and Design*, 2007, 82(15–24): 2047–2054
- Irawan A, Nonami K. Optimal impedance control based on body inertia for a hydraulically driven hexapod robot walking on uneven and extremely soft terrain. *Journal of Field Robotics*, 2011, 28(5): 690–713
- Santos P G D, Garcia E, Cobano J A, et al. SIL06: A six-legged robot for humanitarian de-mining tasks. In: *Proceedings of World Automation Congress*. Seville: IEEE, 2004, 15: 523–528
- Kashiri N, Baccelliere L, Muratore L, et al. CENTAURO: A hybrid locomotion and high power resilient manipulation platform. *IEEE Robotics and Automation Letters*, 2019, 4(2): 1595–1602
- Yang H, Krut S, Pierrot F, et al. On the design of mobile parallel robots for large workspace applications. In: *Proceedings of ASME 2011 International Design Engineering Technical Conferences and Computers and Information in Engineering Conference*. Volume 6: 35th Mechanisms and Robotics Conference, Parts A and B. Washington, D.C.: ASME, 2011, 767–776
- Yang H, Krut S, Baradat C, et al. Locomotion approach of REMORA: A reconfigurable mobile robot for manufacturing Applications. In: *Proceedings of 2011 IEEE/RSJ International Conference on Intelligent Robots and Systems*. San Francisco: IEEE, 2011: 5067–5072
- Rushworth A, Axinte D, Raffles M, et al. A concept for actuating and controlling a leg of a novel walking parallel kinematic machine tool. *Mechatronics*, 2016, 40: 63–77
- Olarra A, Axinte D, Uriarte L, et al. Machining with the WalkingHex: A walking parallel kinematic machine tool for in situ operations. *CIRP Annals*, 2017, 66(1): 361–364
- Li Y G, Liu H T, Zhao X M, et al. Design of a 3-DOF PKM module for large structural component machining. *Mechanism and Machine Theory*, 2010, 45(6): 941–954
- Tunc L T, Shaw J. Experimental study on investigation of dynamics of hexapod robot for mobile machining. *International Journal of Advanced Manufacturing Technology*, 2016, 84: 817–830
- Barnfather J D, Goodfellow M J, Abram T. Positional capability of a hexapod robot for machining applications. *International Journal of Advanced Manufacturing Technology*, 2017, 89(1–4): 1103–1111
- Huang T, Wang P F, Zhao X M, et al. Design of a 4-DOF hybrid

- PKM module for large structural component assembly. *CIRP Annals*, 2010, 59(1): 159–162
22. Pan Y, Gao F. Kinematic Performance Analysis for Hexapod Mobile Robot Using Parallel Mechanism. In: *Proceedings of ASME 2014 International Design Engineering Technical Conferences and Computers and Information in Engineering Conference*. Volume 5A: 38th Mechanisms and Robotics Conference. Buffalo: ASME, 2014, V05AT08A089
 23. Chen Z J, Gao F, Pan Y. Novel door-opening method for six-legged robots based on only force sensing. *Chinese Journal of Mechanical Engineering*, 2017, 30(5): 1227–1238
 24. Zhao Y, Gao F, Hu Y. Novel method for six-legged robots turning valves based on force sensing. *Mechanism and Machine Theory*, 2019, 133: 64–83
 25. Rao A B K, Rao P V M, Saha S K. Workspace and dexterity analyses of hexaslide machine tools. In: *Proceedings of International Conference on Robotics and Automation*. Taipei: IEEE, 2003, 3: 4104–4109
 26. BS EN ISO 9283:1998 *Manipulating Industrial Robots—Performance Criteria and Related Test Methods*. 1998